nature biomedical engineering

ARTICLES

https://doi.org/10.1038/s41551-018-0300-4

Bioresorbable pressure sensors protected with thermally grown silicon dioxide for the monitoring of chronic diseases and healing processes

Jiho Shin[1,2,19], Ying Yan[3,19], Wubin Bai[4,5,19], Yeguang Xue[4,6], Paul Gamble[3], Limei Tian[7], Irawati Kandela[8], Chad R. Haney[9], William Spees[10], Yechan Lee[1,2], Minseok Choi[1,2], Jonathan Ko[1,2], Hangyu Ryu[1,2], Jan-Kai Chang[2,11], Maryam Pezhouh[12], Seung-Kyun Kang[13], Sang Min Won[2,14], Ki Jun Yu[15], Jianing Zhao[2,16], Yoon Kyeung Lee[17], Matthew R. MacEwan[3], Sheng-Kwei Song[10], Yonggang Huang[4,6], Wilson Z. Ray[3]* and John A. Rogers[4,5,18]*

Pressures in the intracranial, intraocular and intravascular spaces are clinically useful for the diagnosis and management of traumatic brain injury, glaucoma and hypertension, respectively. Conventional devices for measuring these pressures require surgical extraction after a relevant operational time frame. Bioresorbable sensors, by contrast, eliminate this requirement, thereby minimizing the risk of infection, decreasing the costs of care and reducing distress and pain for the patient. However, the operational lifetimes of bioresorbable pressure sensors available at present fall short of many clinical needs. Here, we present materials, device structures and fabrication procedures for bioresorbable pressure sensors with lifetimes exceeding those of previous reports by at least tenfold. We demonstrate measurement accuracies that compare favourably to those of the most sophisticated clinical standards for non-resorbable devices by monitoring intracranial pressures in rats for 25 days. Assessments of the biodistribution of the constituent materials, complete blood counts, blood chemistry and magnetic resonance imaging compatibility confirm the biodegradability and clinical utility of the device. Our findings establish routes for the design and fabrication of bioresorbable pressure monitors that meet requirements for clinical use.

Measurements of pressure in organ systems such as the brain, eyes, bladder and blood vessels form an essential diagnostic basis for the assessment of patient health and progression of diseases such as traumatic brain injury, hydrocephalus (intracranial pressure), glaucoma (intraocular pressure) and hypertension (blood pressure). Therefore, the capacity for precise, continuous monitoring of pressure can be critically important in defining treatment protocols that decrease the rate of morbidity and increase the pace of recovery[1–3]. Conventional sensor technologies designed for this purpose are available in the form of accurate, implantable devices that must be surgically extracted following clinical use. These procedures are costly and they expose the patient to additional risks of complications[4]. The devices can also serve as a nidus for infection[5,6] and immune-mediated inflammatory responses[7]. Emerging classes of bioresorbable electronic sensor systems have the potential to address these disadvantages. Here, all of the constituent materials dissolve in biofluids over well-defined periods of time, with biologically benign end-products. This process naturally eliminates the devices after a useful functional period, thereby bypassing the need for surgical extraction. Examples of bioresorbable devices in recent literature include biophysical sensors of pressure, temperature, flow rate and motion[8,9], as well as several types of biochemical markers[8,10]. Additional components range from thermal actuators[8] to neural electrodes[11,12], power supplies[13] and controlled drug-delivery vehicles[14,15]. Published animal model studies include deployments in the intracranial, intra-abdominal and leg cavities[8]; on cortical surfaces[11,12] and in subdermal regions[15,16].

[1]Department of Chemical and Biomolecular Engineering, University of Illinois at Urbana–Champaign, Urbana, IL, USA. [2]Frederick Seitz Materials Research Laboratory, University of Illinois at Urbana–Champaign, Urbana, IL, USA. [3]Department of Neurological Surgery, Washington University School of Medicine, St Louis, MO, USA. [4]Department of Materials Science and Engineering, Northwestern University, Evanston, IL, USA. [5]Center for Bio-Integrated Electronics, Northwestern University, Evanston, IL, USA. [6]Departments of Mechanical Engineering and Civil and Environmental Engineering, Northwestern University, Evanston, IL, USA. [7]Beckman Institute for Advanced Science and Technology, University of Illinois at Urbana–Champaign, Urbana, IL, USA. [8]Developmental Therapeutics Core, Northwestern University, Evanston, IL, USA. [9]Center for Advanced Molecular Imaging, Northwestern University, Evanston, IL, USA. [10]Biomedical Magnetic Resonance Laboratory, Mallinckrodt Institute of Radiology and Hope Center for Neurological Disorders, Washington University School of Medicine, St. Louis, MO, USA. [11]Department of Materials Science and Engineering, University of Illinois at Urbana–Champaign, Urbana, IL, USA. [12]Northwestern Medicine, Feinberg School of Medicine, Northwestern University, Evanston, IL, USA. [13]Department of Bio and Brain Engineering, Korea Advanced Institute of Science Technology, Daejeon, Republic of Korea. [14]Department of Electrical and Computer Engineering, University of Illinois at Urbana–Champaign, Urbana, IL, USA. [15]School of Electrical and Electronic Engineering, Yonsei University, Seoul, Republic of Korea. [16]Department of Mechanical Science and Engineering, University of Illinois at Urbana–Champaign, Urbana, IL, USA. [17]Department of Materials Science and Engineering, Seoul National University, Seoul, Republic of Korea. [18]Departments of Biomedical Engineering, Chemistry, Mechanical Engineering, Electrical Engineering and Computer Science, and Neurological Surgery, Simpson Querrey Institute for Nano/biotechnology, McCormick School of Engineering and Feinberg School of Medicine, Northwestern University, Evanston, IL, USA. [19]These authors contributed equally: Jiho Shin, Ying Yan, Wubin Bai. *e-mail: rayz@wudosis.wustl.edu; jrogers@northwestern.edu

Although recently reported bioresorbable pressure sensors have comparable sensitivity and accuracy to those of conventional, non-resorbable analogues, they offer stable operation over a period of only several days, which is insufficient for many applications[8,9]. Extending this operational lifetime to several weeks demands solutions to daunting challenges in materials science and device design that follow directly from the requirement that the systems must ultimately dissolve completely, at a molecular level, without adverse effect. This difficulty is inherent to all classes of implantable, bioresorbable systems because immersion in biofluids immediately initiates processes of bioresorption. The most effective method to prolong their lifetimes relies on passive encapsulating layers that delay the time at which biofluids come into contact with the active materials. Bioresorbable polymers such as silk fibroin[15,16], poly(*L*-lactide)[9] and poly(lactic-co-glycolic acid) (PLGA)[13] are attractive for such purposes, partly because they can be formed easily by spin-coating or moulding. However, the hydrophilic nature of these materials leads to swelling and water permeation, thereby causing premature fracture, buckling and/or dissolution of the underlying materials. Inorganic alternatives such as silicon dioxide[17,18], silicon nitride[18] and various metal oxides[19] formed by chemical or physical vapour deposition offer exceptionally slow rates of dissolution without these other adverse behaviours. Nevertheless, such materials are of limited practical utility due to extreme difficulties in forming coatings without micro- or nanocracks, pinholes or other defects that can allow water to pass.

Recent work demonstrates that thermally grown layers of silicon dioxide (t-SiO_2) on device-grade silicon wafers can serve as biofluid barriers with defect-free, materials-level perfection over large areas[20,21]. Systematic studies show that the eventual failure results from hydrolysis reactions, as opposed to water permeation through the material or through defects in the films. Specifically, t-SiO_2 dissolves in simulated biofluids at physiological temperatures with rates of several hundredths of a nanometre per day, to yield silicic acid as a bioresorbable end-product[18,20,21]. These observations suggest that the use of ultrathin films of t-SiO_2 as bioresorbable encapsulation layers may enable stable operating periods of weeks or longer. This materials strategy has the potential to yield devices that can address the lifetime requirements for many envisioned clinical applications, such as monitoring of pressure for traumatic brain injury (up to one week)[22] and glaucoma (several months). The principal design approach includes: (1) t-SiO_2 barriers that prevent interactions with biofluids throughout the desired monitoring period, but are sufficiently thin to allow complete bioresorption within a reasonable time frame, typically less than a year; (2) structural components that dissolve in a manner that does not affect the measurement accuracy and (3) interlayer bonding techniques that prevent interfacial water penetration from the periphery.

Here, we demonstrate materials, device structures and fabrication methods that adhere to this strategy. The overall scheme relies on bonding of a pair of silicon-on-insulator (SOI) wafers using adhesion layers of amorphous silica formed by calcination of poly(dimethylsiloxane) (PDMS). Elimination of the handle wafers after bonding yields ultrathin, inorganic bioresorbable electronic devices with robust biofluid barriers that allow stable operation over extended periods of time. Data on the biodistribution of dissolved silicon in mice at five weeks following implantation of intracranial sensors formed in this manner, together with assessments of the haematology (complete blood count), blood chemistry and magnetic resonance imaging (MRI) compatibility, confirm their biodegradability and clinical utility. Measurements of intracranial pressures in rats over 25 days illustrate high accuracy and low drift, with an overall performance that compares favourably to that of non-resorbable clinical standards. The results not only establish routes to bioresorbable pressure monitoring technologies that meet requirements for clinical use, but they also serve as a generalizable platform for broad classes of bioresorbable electronic devices that can offer stable operating characteristics over long periods of time.

Results and discussion

Materials, designs and fabrication procedures. Figure 1a shows a schematic illustration of an inorganic bioresorbable pressure sensor based on four silicon nanomembrane (Si NM; 200 nm) sensors (length: ~300 μm; width: ~8 μm), two of which serve as strain gauges and two as temperature gauges. Partial extension of the strain gauges over an air-filled cavity (200 μm × 200 μm × 10 μm) yields a floating, pressure-sensitive diaphragm with a piezoresistive response in the strain gauge that depends on the mechanical equilibrium between the pressure of the surroundings and that of the air trapped inside the cavity. The temperature gauges, which are not located on the diaphragm and therefore are unresponsive to changes in pressure, respond to changes in the surrounding temperature via their temperature-dependent resistance. The red and blue insets illustrate the layer composition in regions of the diaphragm with and without the strain gauge, respectively. The diaphragm consists of a tri-layer of t-SiO_2 (~10 nm), monocrystalline Si (~200 nm) and electron-beam evaporated SiO_2 (eb-SiO_2; ~600 nm; see Supplementary Fig. 1 for scanning electron microscopy cross-sections). The t-SiO_2 layer insulates the Si devices from exposure to biofluids, thereby extending their functional lifetime. The eb-SiO_2 layer constitutes the thickest part of the diaphragm and serves to increase the vertical separation between the neutral mechanical planes of the strain gauges and the bulk membrane, thereby improving the response of the strain gauges to pressure. Four exposed regions of the Si NMs serve as openings for contact pads (200 μm × 200 μm) to allow electrical connection with a data acquisition system; the rest of the device surface is protected by the t-SiO_2 layer.Four exposed regions of the

A photograph and optical micrograph of a representative device, with a size and weight of 1.3 mm × 1.3 mm × 16 μm and ~60 μg, respectively, appear in Fig. 1b,c. Figure 1d shows a circuit diagram of the pressure sensor in which four gauges combine to form a Wheatstone bridge to compensate for temperature effects on the piezoresistive response of the strain gauges[23]. A magnified view of the diaphragm in Fig. 1e demonstrates the isolation of the strain gauges (pink) by regions where the Si NM (width: ~5 μm) is removed (grey lines). The diaphragm has an area of 200 μm × 200 μm, defined by the lateral dimensions (boundary lines) of the trench.

Figure 1f and Supplementary Fig. 2 illustrate the fabrication steps, beginning with the formation of Si NM sensors on a SOI wafer (SOI-A; top Si: ~200 nm, buried SiO_2: ~1 μm, Si wafer: ~100 μm) via solid-state diffusion of phosphorus at 950 °C, photolithography and reactive-ion etching (RIE) to define strain gauges and temperature gauges from the top Si, and evaporation to form the eb-SiO_2. Photolithography and inductively coupled plasma deep reactive-ion etching (ICP-DRIE) then create an array of holes (100 μm × 100 μm) through the thickness of the wafer to release gaseous products of the calcination process (step 1). Patterning and etching of the top Si layer of a second SOI wafer (SOI-B; top Si: ~15 μm, buried SiO_2: ~600 nm, Si wafer: ~85 μm) creates a trench (step 2). Spin-coating of a thin layer of PDMS onto SOI-B allows it to bond to SOI-A via thermal curing while pressure is applied with a steel vice (see Supplementary Note 1 and Supplementary Fig. 3 for analysis of errors associated with PDMS coating on the inner surfaces of the trench).

Heating the vice in a furnace at 550 °C for 2 h calcines the PDMS adhesion interlayer to yield an amorphous silica material (~200 nm) via a thermal oxidative degradation process[24]. Gaseous by-products, such as carbon dioxide and water, escape the bonding interface via the vent holes, leaving behind a smooth film of silica (see Supplementary Note 2 and Supplementary Fig. 4 for details on the technique). Supplementary Figs. 5a,b show scanning electron and atomic force microscopy images of the silica layer. A single

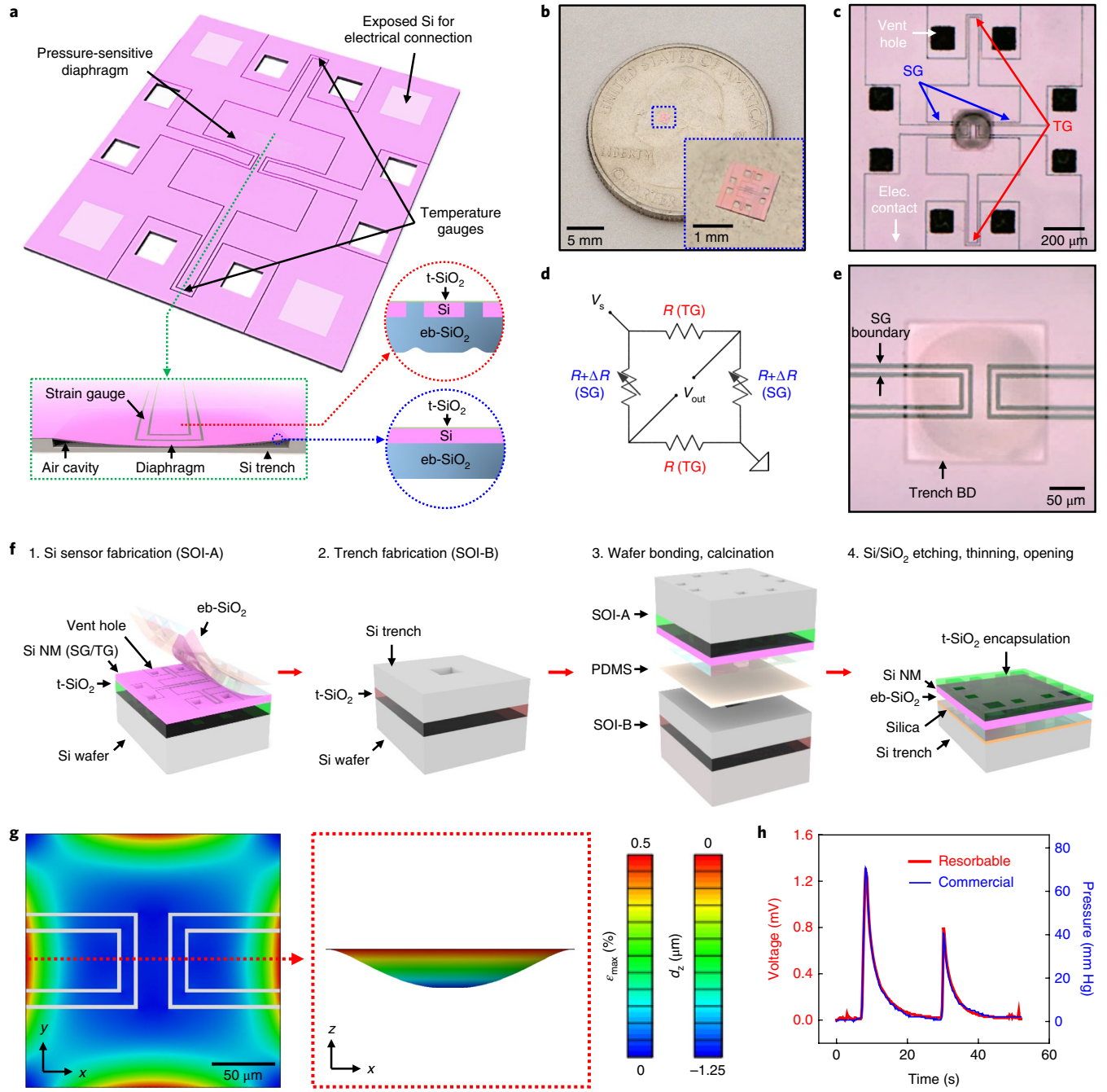

Fig. 1 | Materials and designs for long-lived, inorganic bioresorbable pressure sensors. a, Schematic illustration of a bioresorbable pressure sensor composed of layers of monocrystalline silicon and silicon dioxides, formed by thermal oxidation (t-SiO_2) or electron-beam evaporation (eb-SiO_2). Silicon nanomembrane strain gauges on a flexible diaphragm capture pressure variations via the piezoresistive response of silicon, whereas temperature gauges react to temperature changes via temperature-dependent resistance. Inset: cross-section across the diaphragm (green) revealing the air cavity and silicon trench located underneath. The cross-sections across strain gauge (red inset) and non-strain gauge (blue) regions show the tri-layer composition. **b**, Photograph of a device placed on a quarter. The inset presents a magnified view of the sensor. **c**, Optical micrograph of the sensor. Two pairs of strain and temperature gauges combine to form a Wheatstone bridge circuit. **d**, Circuit diagram of a Wheatstone bridge, consisting of strain gauges, temperature gauges, a voltage source and a meter that compensates for temperature-induced variations in the piezoresistivity of strain gauges. *R* represents the gauge resistance. **e**, Optical micrograph of strain gauges embedded in a diaphragm. Two boundary lines (grey; no silicon) isolate the strain gauges (pink; silicon) from the surrounding Si NM. **f**, Steps for fabricating bioresorbable pressure sensors: (1) The formation of silicon sensors on a SOI wafer, SOI-A. (2) The fabrication of silicon trench on a separate SOI wafer, SOI-B. (3) Aligned bonding of SOI-A and SOI-B using a PDMS adhesion interlayer (beige), followed by calcination of the PDMS to yield amorphous silica. (4) The elimination of silicon wafers, thinning of buried oxide layers and patterned exposure of Si NM for the electrical contacts. Thicknesses are not to scale. **g**, Three-dimensional finite-element analysis results for the distribution of principal strains (left) and vertical displacements (right) of the diaphragm under an external pressure of 40 mm Hg above atmospheric. ε_{max} and d_z are the principal strain and vertical displacement, respectively. **h**, Responses of a bioresorbable pressure sensor (red; $V_s = 2.5$ V) and a commercial sensor (blue) to time-varying pressures. SG, strain gauge; TG, temperature gauge.

broad peak near −110 ppm in the ^{29}Si NMR spectrum of the silica (Supplementary Fig. 5c) confirms the full conversion of PDMS (no peak around −21 ppm, where $SiO_2(CH_3)_2$ would appear) into amorphous SiO_2 (Si-(O-Si)$_4$, Q_4 site). Electron dispersive spectroscopy also confirms the absence of carbon (Supplementary Fig. 5d; step 3). A series of ICP-DRIE and wet etching (in buffered oxide etchant) processes removes the handle wafers, reduces the thickness of the t-SiO_2 layer to a desired value (~10 nm) and exposes the Si NM for electrical contact (step 4).

Device characterization. Three-dimensional finite-element analysis provides insights into the mechanics of pressure sensing using these constructs. The principal strain distributions and the vertical displacements associated with the diaphragm under an external pressure of 40 mm Hg above atmospheric appear in Fig. 1g. The maximum strain for any applied pressure across the range of interest occurs along the edge of the trench, where the strain gauges are located. The relationship between the resistance of a strain gauge and pressure is linear with a slope of $-0.13\,\Omega\,mm\,Hg^{-1}$, which corresponds to a gauge factor of about −20.9, consistent with theory (see Supplementary Figs. 6a–c and Supplementary Note 3). The modest value of the gauge factor follows from the heavy doping of the top silicon needed to allow phosphorus atoms to diffuse through its thickness to the base (Supplementary Fig. 6d), at the location of electrical contact pads formed as a result of wafer bonding and etching[25,26]. The pressure sensitivity can be improved by reducing the thickness of the Si NM, increasing the area of the diaphragm and introducing serpentine designs for the strain gauges (Supplementary Figs. 6e,f). Measurements of the resistance of the temperature gauge as a function of temperature reveal a linear response with a temperature coefficient of resistance of $0.0012\,°C^{-1}$, which lies within the range of expected values for monocrystalline silicon (Supplementary Fig. 6g)[26,27]. Changes in pressure sensitivity, due to changes in temperature within the relevant ranges for the intracranial space (34–40 °C), induce errors that are less than ±0.4 mm Hg (Supplementary Fig. 6h).

In vitro evaluations that mimic thermodynamic conditions inside the intracranial space illustrate the functional capabilities of the device. An airtight plastic chamber filled with artificial cerebrospinal fluid (ACSF; pH 7.4) at physiological temperature (37 °C), and connected via tubes to a commercial pressure sensor and a syringe allows the measurement and control of pressure, respectively (Supplementary Figs. 7a,b). Comparison of the voltage responses of the sensor (red; $V_s = 2.5$ V) with the measured pressures (blue) for values over a range relevant to intracranial monitoring reveal a linear correspondence (Fig. 1h and Supplementary Fig. 7c). The level of noise in the response of the bioresorbable sensor, evaluated as the difference between the pressures measured by bioresorbable and commercial sensors (noise floor less than ±0.8 mm Hg), lies within ±1 mm Hg of the 0–30 mm Hg range and ±3 mm Hg of the measured values that exceed this range (Supplementary Fig. 7d). These numbers meet the intracranial pressure (ICP) monitoring standards defined by the Association for the Advancement of Medical Instrumentation (that is, a functional range of 0–100 mm Hg, an accuracy of ±2 mm Hg in the 0–20 mm Hg range and a maximum error less than ±10% of the 20–100 mm Hg range)[28]. Comprehensive results from continuous in vitro operation over a period of 22 d reveal variations in pressure sensitivity and baseline within ±1.5% and ±2.5 mm Hg, respectively (Supplementary Figs. 7e,f). The observed baseline drift is in the range specified for clinical ICP monitors (that is, ±2 mm Hg maximum in the first 24 h and ±1 mm Hg per day thereafter)[29].

Kinetics of dissolution. The key feature of this system is that the constituent materials are water soluble, with biocompatible end-products. The dissolution of Si and SiO_2 yields silicic acid, $Si(OH)_4$, via hydrolysis, according to $Si + 4H_2O \rightarrow Si(OH)_4 + 2H_2$ and $SiO_2 + 2H_2O \rightarrow Si(OH)_4$, respectively. Figure 2a shows the kinetics, evaluated as changes in the thicknesses of the silicon oxide films obtained by thermal oxidation, electron-beam evaporation and PDMS calcination in ACSF at 37 °C. The thicknesses of the t-SiO_2 and eb-SiO_2 layers can be quantified by spectroscopic reflectometry, whereas those of the silica adhesion layer can be assessed most effectively by profilometry, due to non-uniformities in film thickness that result from calcination. Supplementary Fig. 8 shows the steps for fabricating arrays of square patterns of silica used in the study, along with an image of these structures. The layers of t-SiO_2, eb-SiO_2 and silica dissolve at rates of 0.11 ± 0.01, 13.6 ± 1.6 and $129 \pm 9\,nm\,d^{-1}$, respectively. The rates of dissolution of single-crystalline silicon and bioresorbable metals (Mo, Mg) appear in earlier studies[8,11]. These rates, together with the overall structures of the devices, yield estimated times for full dissolution of around 400 days. By decreasing the thickness of the Si trench to ~10 μm (trench depth ~5 μm, thickness of silicon support under the trench ~5 μm, for example), this time can be reduced to approximately 290 days without significantly compromising the sensor response.

Figure 2b shows a schematic illustration of a set-up designed to test the dissolution of bioresorbable sensors at accelerated rates by immersion in PBS (pH 7.4) at 95 °C in a plastic bottle. Employing a test design in which the sensor uses a Si wafer with a layer of t-SiO_2 on top as a substrate allows unidirectional thinning of the component layers in sequence from top to bottom. Figure 2c presents optical micrographs collected at various stages of dissolution. The complete hydrolysis of the t-SiO_2 layer leads to exposure of the Si NM within 5 h; fast and non-uniform dissolution of the silicon creates a rough surface profile, which appears as dark regions under the microscope. The eb-SiO_2 and silica adhesion layers disappear within 20 h, followed by the Si trench (outer grey region) within 80 h. Complete disintegration leaves only the surface of the t-SiO_2 substrate with a shallow surface relief (pink).

The use of t-SiO_2 as a defect-free barrier to prevent biofluid penetration of the Si device layer is critically important to the robust, long-lived operation. The functional lifetime is proportional to the thickness of the t-SiO_2 (Fig. 2d)[20]. The calibration curves of a bioresorbable pressure sensor (~10 nm t-SiO_2) collected at regular time intervals after immersion of the device in PBS at 95 °C indicate highly uniform pressure responsivity in the first 3 h followed by rapid transience. After the dissolution of the t-SiO_2, the device undergoes failure due to pinpoint penetration of water through eb-SiO_2 regions (along strain gauge boundary lines) of the diaphragm, which leads to the formation of cracks and disintegration (Fig. 2e).

In vivo biodistribution and biocompatibility. Evaluation of the biodistribution of dissolved silicon, the haematology (complete blood count) and the blood chemistry of mice implanted with bioresorbable intracranial sensors provides insights into the physiological reactions of these devices as bioresorbable implants. The use of miniaturized devices (size: 750 μm × 750 μm × 11 μm; weight: ~12 μg) without t-SiO_2 encapsulation accelerates the dissolution, thereby facilitating assessments over a five-week period of study. The surgical procedure includes opening a craniectomy defect that penetrates through the dura, implanting the sensor and sealing the intracranial cavity using a drop of bioresorbable tissue adhesive.

Figure 3a shows the concentrations of silicon in liver, spleen, heart, kidney, brain and lung tissues explanted from mice at one, three and five weeks after implantation, measured by inductively coupled plasma optical emission spectrometry (see Methods for sample preparation steps). The results indicate higher concentrations of silicon in the spleen, heart and lungs compared with the brain, where the device is located, one week after implantation. This observation can be attributed to the fast turnover of cerebrospinal fluid volumes in mice (12–13 times per day in mice; 3–4 times per

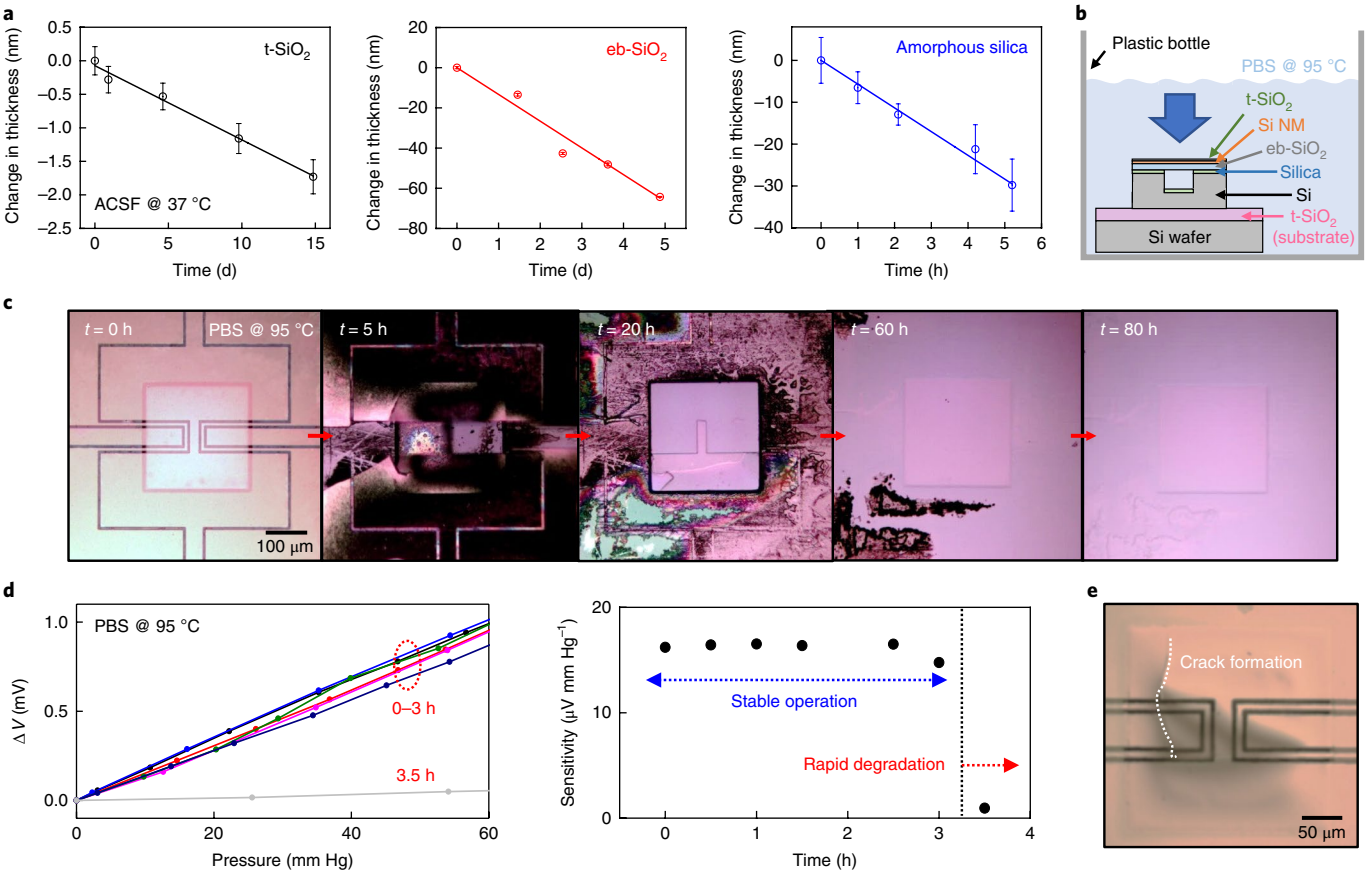

Fig. 2 | Kinetics of dissolution of a bioresorbable pressure sensor. a, Measured changes in thickness as a function of the immersion time of t-SiO_2 (left), eb-SiO_2 (middle) and amorphous silica (obtained from the calcination of PDMS; right) in ACSF (pH 7.4) at 37 °C. The dissolution rates are 0.11 ± 0.01, 13.6 ± 1.6 and 129 ± 9 nm d^{-1}, respectively. Circles and error bars represent the mean ± s.e.m. for ten measurements. **b**, Schematic illustration of the in vitro dissolution experiment set-up. The blue arrow indicates the angle of the optical microscope imaging. **c**, Optical micrographs at various stages of the accelerated dissolution of a bioresorbable pressure sensor due to its immersion in PBS (pH 7.4) at 95 °C. **d**, Voltage response of a sensor with t-SiO_2 encapsulation (~10 nm) and comparison to a commercial device at various times after immersion in PBS at 95 °C (left), with the corresponding responsitivities as a function of time (right). The data indicate two-stage kinetics in function, involving stable operation for several hours as determined by the dissolution of the t-SiO_2 encapsulation layer, followed by rapid degradation due to the formation of holes/cracks in the diaphragm owing to the dissolution of the functional layers. **e**, Optical micrograph of a cracked diaphragm.

day in humans)[30]. The cerebrospinal fluid circulates through the brain, then joins the bloodstream by bulk reabsorption via arachnoid villi, transporting dissolved silicic acids to other organs. Mononuclear phagocyte system-related organs such as the liver, spleen and lung have phagocytic cells that uptake nanomaterials in the blood, leading to the deposition of silicon in these organs[31]. The clearance of silicic acid from the body, via excretion through the kidneys, leads to a gradual decrease and nearly complete removal from most organs after five weeks. However, abnormal levels of silicon in the kidney and brain at week five suggest the presence of residual device silicon in the brain, as verified by computed tomography images in Fig. 3b. Scans of the mouse brain along the sagittal, coronal and axial planes reveal the locations of the craniectomy defect and a sensor implanted near the top surface of the brain, fixed at a tilted angle, five weeks post-implantation.

The results of the complete blood count and blood chemistry tests provide a comprehensive understanding of the health of the mice (Fig. 3c,d). The average counts of white blood cells, red blood cells, platelets, and the levels of haemoglobin and hematocrit (the percentage of red blood cells in blood) show no significant differences between implanted mice and control animals throughout the five-week period of the studies. Blood levels of enzymes and electrolytes, which serve as indicators of organ-specific diseases, also fall within the confidence intervals of control values. For example, normal levels of alanine aminotransferase, cholesterol and triglyceride, phosphorus and urea nitrogen, calcium, albumin and total proteins indicate the absence of disorders in the liver, heart, kidney, bone and nerve, and good overall health, respectively. The complete results for both tests appear in Supplementary Figs. 9a,b.

Supplementary Fig. 9c compares changes in the body weight of mice implanted with intracranial sensors to those of control animals. The differences are minimal, indicating continued maturation without toxic effects. Histopathologic evaluation of tissues obtained from a control mouse and a mouse implanted with a sensor for five weeks reveals the absence of inflammation, ischaemia/tissue necrosis and other architectural/histologic abnormalities in the major organs (brain, spleen, heart, kidney, lung and liver) in both mice, either grossly or by microscopic examination (see Fig. 3e and Supplementary Fig. 9d for representative images).

In vivo monitoring of ICP. Acute and chronic tracking of intracranial temperature (ICT) and ICP in rats demonstrate the accuracy and long operating lifetimes of the bioresorbable sensors. Figure 4a and Supplementary Fig. 10a illustrate the procedures for implantation, which involve opening a craniotomy defect, placing the sensor

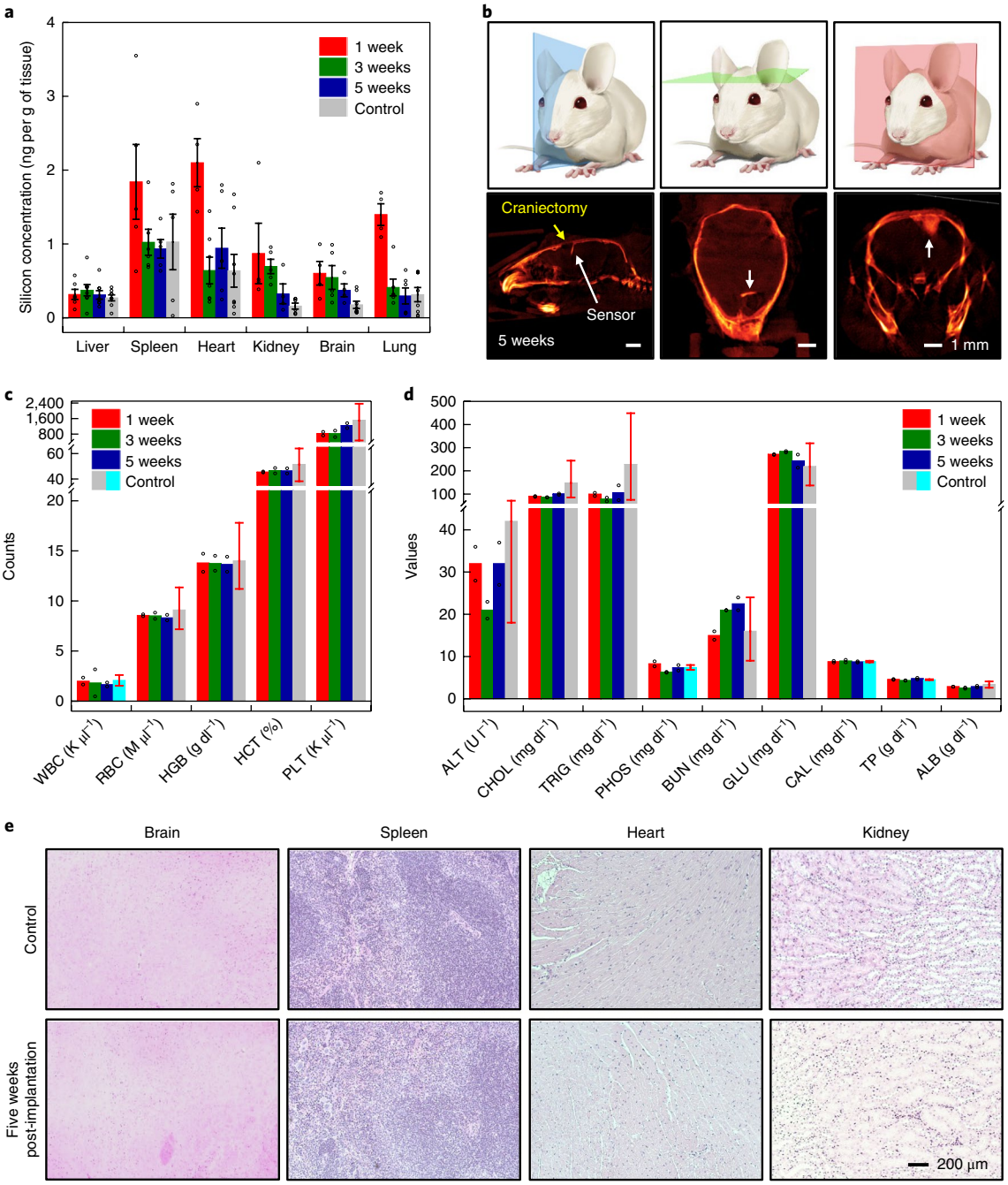

Fig. 3 | In vivo measurements of the elemental biodistribution and biocompatibility of bioresorbable devices throughout their functional lifetimes and beyond. a, Biodistribution of dissolution products of bioresorbable pressure sensors (size: 750 μm × 750 μm × 10 μm; weight: ~12 μg; no t-SiO_2) implanted inside the intracranial spaces of mice (two for each time point) with comparisons to two control mice. The silicon concentrations in organs explanted at one, three and five weeks post-implantation were determined by inductively coupled plasma optical emission spectrometry. The circles are the individual data points, the filled bars indicate the mean and the error bars the s.e.m. for at least four spectrometric measurements. **b**, Computed tomography scans of a mouse brain five weeks post-implantation in the sagittal (left), coronal (middle) and axial (right) planes, showing the locations of the craniectomy and a sensor near the surface of the brain. **c**,**d**, Results of the complete blood count (**c**) and blood chemistry (**d**) tests for the mice in **a**. No significant differences between control and implanted animals were found for both tests. Control data were provided by the mouse supplier (grey) or collected from 22–24 mice acquired from two batches in a span of two months (cyan). Circles, bars and error bars represent individual data points, the mean and 95% confidence intervals, respectively. WBC, white blood cell; RBC, red blood cell; HGB, blood haemoglobin level; HCT, hematocrit level; PLT, platelet count in blood; ALT, alanine aminotransferase; CHOL, cholesterol; TRIG, triglycerides; PHOS, phosphorus; BUN, urea nitrogen; GLU, glucose; CAL, calcium; TP: total protein; ALB, albumin. **e**, Representative histology of brain, spleen, heart and kidney tissues of a control mouse and a mouse implanted with a bioresorbable sensor five weeks post-implantation.

mounted on a thin film PLGA (~10 μm thick; inset) inside and applying bioresorbable glue to bond the PLGA film with the surrounding skull, thereby sealing the cavity. The insertion of the probe of a standard clinical ICP monitor through a separate defect yields reference data for comparison testing. A plastic protector hat, secured to the rat's skull by transcranial screws and dental cement, protects

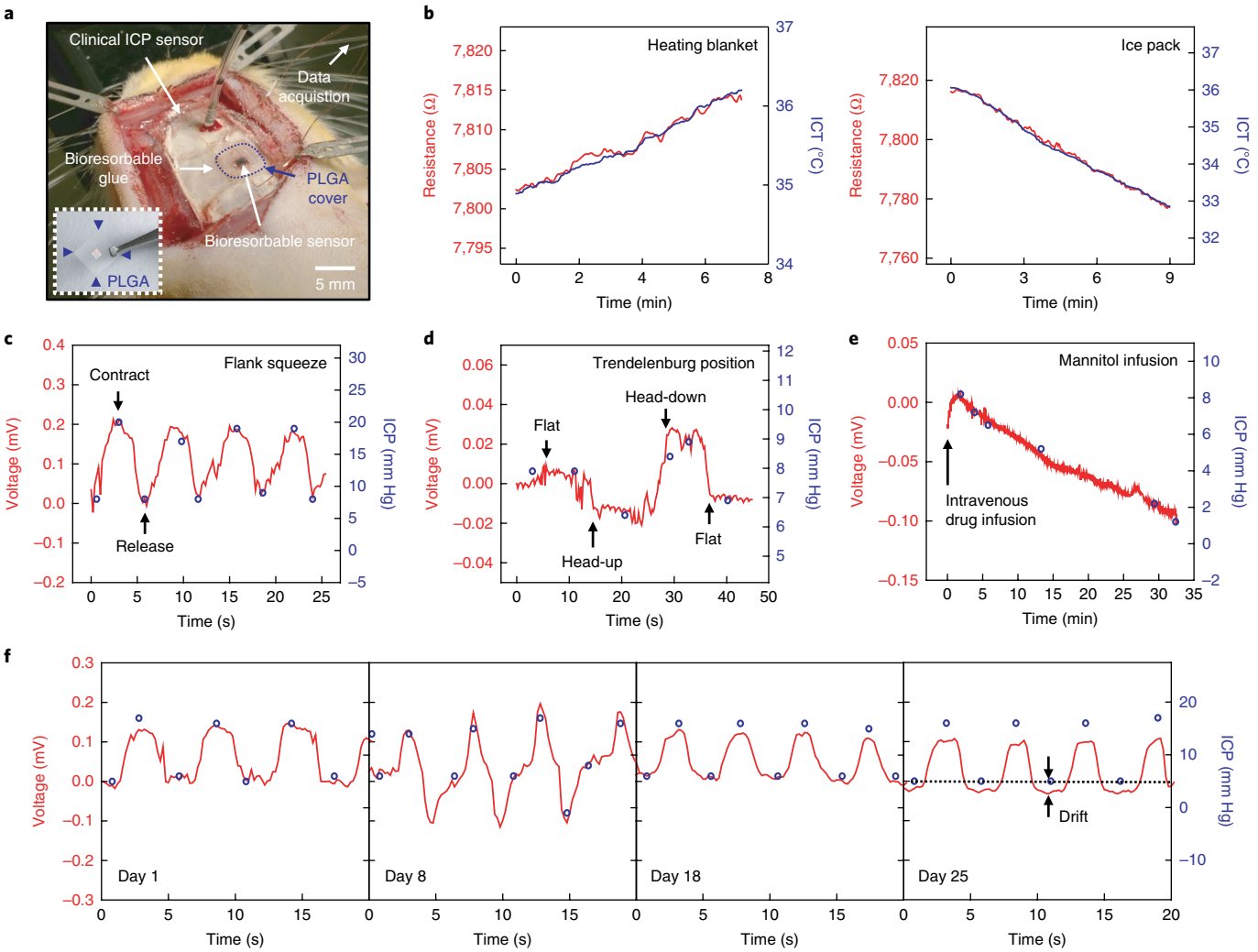

Fig. 4 | Acute and chronic monitoring of intracranial temperature and pressure in rats using bioresorbable sensors. a, Photograph of a bioresorbable ICP sensor, mounted on a thin film of PLGA (~10 μm thick; inset), implanted device-side down in an intracranial cavity of a rat. Bioresorbable glue bonds the edges of the film to the surrounding skull and seals the cavity. Wired connection to a digital multimeter allows data acquisition from the sensor. A clinical ICP monitor probe inserted in the same hemisphere of the brain serves as a reference. **b**, In vivo recordings of the ICT of a rat as a function of time. Both bioresorbable (red) and commercial (blue) devices record a gradual increase (left) and decrease (right) in ICT caused by the application of a heating blanket or an ice pack. **c**–**e**, In vivo monitoring of variations in ICP due to contracting and releasing rat's flank (**c**), laying in Trendelenburg (30° head-down, **d**) and reverse Trendelenburg (30° head-up, **e**) positions, and infusing mannitol in the saphenous vein, as a function of time by both bioresorbable (red) and commercial (blue) sensors. **f**, In vivo recordings of ICP as a function of time on days 1, 8, 18 and 25 post-implantation. Compressing and releasing the flank induce variations in ICP. Recordings on day 25 show ~3 mm Hg negative drift for the bioresorbable device.

all of the device components throughout the monitoring period to enable long-term, repeated measurements (Supplementary Figs. 10b–d). All in vivo data in Fig. 4 rely on direct wire connections (Supplementary Fig. 10c, left) to an external digital multimeter to record voltage. Wireless data acquisition is also possible by using a miniaturized wireless potentiostat (Supplementary Fig. 10c, right) that can wirelessly transmit resistance data to a computer-based station (see Supplementary Figs. 10e,f for representative data)[8].

Figure 4b shows acute recordings of the ICT by both a bioresorbable device (red) and a commercial thermistor (blue) during gradual heating (using an electrical heating blanket) and cooling (using an ice pack) of the animal, indicating similar levels of accuracy. Figures 4c–e demonstrate recordings of acute variation in ICP induced by contracting and releasing the rat's flank (Fig. 4c), laying the rat in the Trendelenburg (30° head-down) and reverse Trendelenburg (30° head-up) positions (Fig. 4d), and intravenously infusing Mannitol (dose: 2 g per kg weight) via the saphenous vein (decreases by 2–5 mm Hg starting ~10 min after infusion; Fig. 4e) using bioresorbable (red) and commercial (blue) ICP sensors. Figure 4f summarizes the ICP signals collected while compressing and releasing the flank on days 1, 8, 18 and 25. The responses of the sensor from days 1 through 18 display absolute accuracy within ± 2 mm Hg and baseline drift within ±1 mm Hg. The recordings on day 25 show approximately 4 mm Hg negative drift, in a range consistent with that of clinical ICP monitors after several days of implantation without re-calibration[29,32–34]. The signals from the device disappear after day 25, possibly due to the dissolution of the bioresorbable metal pads following the penetration of water into the sensor-wire interface (see Supplementary Note 4 for more discussion on drift, signal noise and in vivo lifetime of bioresorbable device).

MRI compatibility. In many clinical scenarios, patients require MRI at various stages of recovery. Biomedical implants made of conductive materials and containing loops in electrical circuits can

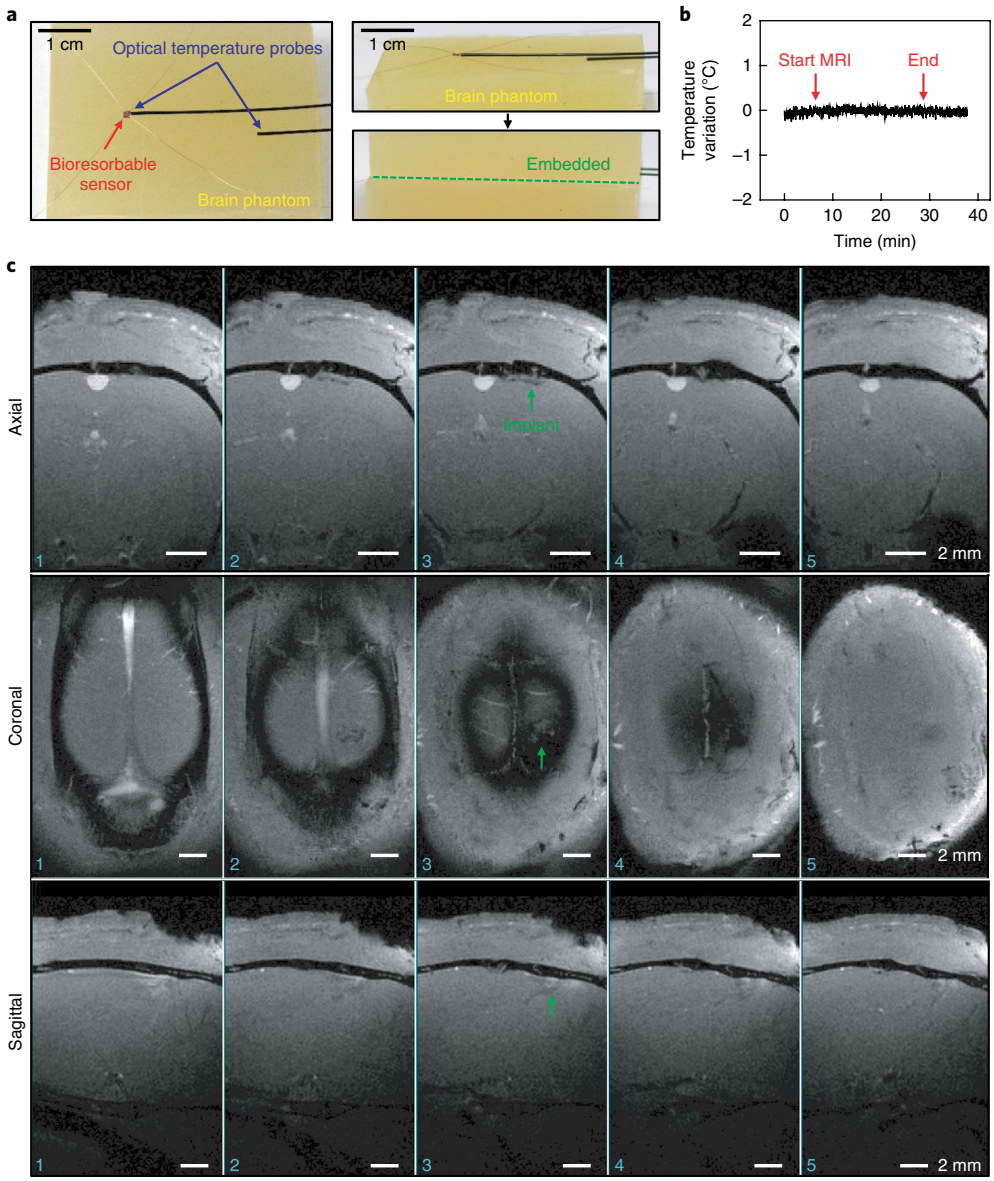

Fig. 5 | MRI compatibility of bioresorbable sensors. a, Photograph of a bioresorbable sensor and two fibre optic temperature probes placed between two slabs of brain phantom, designed to imitate the conductivity and dielectric constant of brain tissue. **b**, Recordings of the difference in temperatures measured by the two probes throughout a 20-min scan, indicating no significant heating of the device. **c**, Representative MRI images of a rat brain implanted with a bioresorbable sensor, taken along the axial, coronal and sagittal planes. Five images in each plane were collected at locations parallel to one another with 0.5 mm separation (slice thickness). Images show no sign of magnetic-susceptibility-related artefacts. The arrows indicate the positions of the sensor.

interact with magnetic and electromagnetic fields of the MRI scanner, causing problems such as device heating and image distortion (due to magnetic susceptibility artefacts). Figure 5 illustrates in vitro and in vivo studies that verify the MRI compatibility of bioresorbable Si-based sensors[35,36].

Figure 5a illustrates the set-up for the in vitro device-heating test, which consists of a bioresorbable sensor and two fibre optic temperature probes, one near the sensor and the other at a distance, embedded between two 2-cm-thick slabs of gel phantoms that are designed to approximate the conductivity and dielectric constant of the brain. Recordings of the difference between temperatures measured by the two probes throughout a continuous 20-min, high specific absorption rate MRI scan suggest that there is no significant heating associated with the presence of the device (Fig. 5b), possibly due to the small size (~500 μm diameter) of the loop that constitutes the Wheatstone bridge circuit. A series of representative in vivo MRI images (0.5-mm-slice thickness) of a rat with an implanted sensor confirm the absence of image distortion (Fig. 5c), possibly due to the low magnetic susceptibility of silicon.

The materials, device structures and fabrication strategies introduced here serve as the foundations for bioresorbable implants capable of accurate, stable monitoring of pressure and temperature for extended periods of operation, previously attainable only through the use of non-resorbable technologies. In vivo experiments to track the elemental biodistribution of silicon, haematology and blood chemistry during and after the processes of bioresorption reveal a lack of any measurable toxic effects or immune reactions. The in vivo monitoring of intracranial pressures in rats over 25 days demonstrates the high level of accuracy that can be obtained, with extremely low baseline drifts due to intrinsic

(materials biodegradation) and extrinsic (temperature fluctuation) effects. These same device concepts and material constructs will enable robust, long-term operation across a broad range of bioresorbable implants, including sensors of motion, flow and various chemical species, and of other components such as stimulators, power supplies and thermal actuators.

Methods

Fabrication of bioresorbable pressure and temperature sensors with thermal SiO_2 layers as biofluid barriers. Mechanical back-grinding (Syagrus Systems) reduced the total thickness of SOI wafers (SOI-A, top Si ~200 nm, buried SiO_2 ~1 μm, Si wafer ~100 μm; SOITEC) before device fabrication. Solid-state diffusion of phosphorus at 950 °C followed by photolithography and RIE (Plasma-Therm RIE) defined the Si NM strain gauges and temperature gauges in the top Si of the SOI-A wafer. Electron-beam evaporation of SiO_2 pellets (99.99%; Kurt J. Lesker Company) formed a layer of SiO_2 (~600 nm) on top. Photolithography and ICP-DRIE (STS Pegasus) defined an array of vent holes (area: 100 μm × 100 μm) through the thickness of SOI-A. Photolithography and ICP-DRIE formed a square trench, with the dimensions: 200 μm × 200 μm × 10 μm, on a separate SOI wafer (SOI-B; top Si: ~15 μm, buried SiO_2: ~600 nm, Si wafer: ~85 μm after mechanical grinding; University Wafer). The wafers were bonded by spin-coating ~3 μm thick layer of PDMS (diluted by mixing part A/part B/hexane in 10:1:100 ratio; Sylgard 184; Dow Corning) on SOI-B, partially curing the PDMS by heating the wafer at 110 °C for 1 min, transferring SOI-A on top of SOI-B in a manner that aligned the strain gauges of SOI-A directly above the trench of SOI-B, pressing the wafers together in a steel vice (Toomaker's vice; Tormach) and fully curing the PDMS by placing the vice in a 70 °C convection oven for 2 h. Heating the vice in a furnace, by raising the temperature to 550 °C over 2 h and keeping it there a further 2 h, converted the PDMS adhesion layer to amorphous silica. Next, ICP-DRIE removed the top Si wafer (SOI-A) of the bonded sample to expose the buried oxide. Wet etching in a buffered oxide etchant (NH_4F:HF = 6:1; Transene Company) reduced the thickness of this oxide to the desired value (~10 nm). Patterned wet etching exposed square areas (~100 μm × 100 μm) of Si NM in the four corners. Profilometer (Alpha Step D-500; KLA-Tencor) measurements confirmed the thickness of the buried oxide, with additional wet etching as needed to reach the desired value. Sputtering a layer of molybdenum (~100 nm), followed by patterning and wet etching formed metal contact pads (area: 150 μm × 150 μm) on top of the four exposed areas of the Si NM. Spin-coating a layer of photoresist on the top surface, etching the handle wafer and buried oxide of SOI-B by ICP-DRIE and wet etching in a buffered oxide etchant, and removing the photoresist by RIE (March RIE) completed the fabrication.

Connections to data acquisition systems. Silver conductive epoxy (MG Chemicals) formed the electrical connections between the molybdenum metal pads of the bioresorbable sensor and the ultrathin enamelled copper wires (~80 μm diameter; Remington Industries). An approximately 100-μm-thick layer of bioresorbable polyanhydride[8] encapsulated the sensor-wire interface to prevent direct exposure to biofluid. Soldering then connected the wires to printed circuit boards with gold pins (DigiKey; Supplementary Fig. 10b, left). Contacting the test hook probes of a digital multimeter (DMM, USB-4065; National Instruments) with the gold pins enabled data acquisition from the sensor with minimal contact resistance. The use of a 6.5-digit resolution setting in the commercially available LabVIEW SignalExpress for DMM software enabled the measurement of small voltage changes of the sensor during all in vitro and in vivo experiments; a lower resolution setting induced noise levels high enough to obscure the actual pressure signal.

Calibration of the pressure response. The absolute pressure calibration of the bioresorbable sensor relied on a custom set-up consisting of an airtight container (Nuovoware) connected by two plastic tubes to a commercial pressure sensor (NUL-210; NeuLog) and a syringe for pressure measurement and control, respectively. Placing the bioresorbable sensor inside the container, which was partially filled with ACSF (pH 7.4; Ecocyte BioSciences), followed by connnection of the wires to a power supply (V_s = 2.5 V) and a digital multimeter (Supplementary Fig. 7a,b) prepared the system for testing. Collecting the voltage response of the bioresorbable device and pressures from the commercial device simultaneously, while varying the fluid pressure by moving the plunger of the syringe in and out, yielded a calibration curve over the range of pressures relevant to intracranial monitoring (0–70 mm Hg, Supplementary Fig. 7c).

Evaluation of the hydrolysis kinetics. Measurements by spectroscopic reflectometry (MProbe; Semiconsoft) defined changes in t-SiO_2 and eb-SiO_2 film thicknesses. Profilometry (Alpha Step) revealed the thicknesses of the square dots (50 μm × 50 μm) of the amorphous silica adhesion interlayer formed on the t-SiO_2 wafers (Supplementary Fig. 8). Each sample had an approximate lateral size of 1 cm × 1 cm, with coatings of t-SiO_2 on the side and bottom surfaces formed by thermal oxidation. The experiments involved placing the sample in a screw cap plastic bottle filled with ~50 ml ACSF solution, storing the bottle in an oven (Fisher Scientific) to maintain the solution temperature near 37 °C and monitoring the temperature throughout the experiment with a digital thermometer probe (DTP482; CDN) penetrating through the plastic cap. The dissolution rates were determined by repeatedly rinsing the sample with deionized water, drying, measuring the sample thickness and placing it back in the solution (renewed every 4 d).

Accelerated soaking tests. To obtain images of a bioresorbable sensor through the various stages of accelerated dissolution, the device was soaked in PBS (pH 7.4; Sigma-Aldrich) at 95 °C for 5, 20, 60 and 80 h, rinsed with deionized water, dried and analysed under an optical microscope. Similarly, the evaluation of the change in the pressure sensitivity of the device throughout the process of thinning of the t-SiO_2 encapsulation layer involved soaking the device in PBS at 95 °C for 30 min, rinsing with deionized water, drying, calibrating against the commercial pressure sensor and placing back in the PBS. The dissolution chamber comprised a screw cap plastic bottle fitted with a penetrating thermometer probe and was kept in a heated oven.

Evaluation of the biodistribution, haematology and blood chemistry of mice. Miniaturized bioresorbable sensors (size: 750 μm × 750 μm × 11 μm; weight: ~12 μg) without t-SiO_2 encapsulation were ultraviolet-radiation-sterilized overnight before device implantation. The implantation procedure involved anaesthetizing a female CD-1 mouse (Charles River) with isoflurane gas, fixing the head in a stereotaxic frame, forming a craniectomy defect using a drill, implanting the sensor into the intracranial cavity, sealing the defect with a drop of bioresorbable tissue adhesive (TissueSeal) and suturing the scalp. These procedures have been approved by The IACUC of Northwestern University. Daily monitoring and weighing of the mice ensured their normal stress and moribund conditions. Computed tomography scans, carried out every week, tracked the size and location of the implanted device. Euthanization of one or two mice at weeks one, three and five after the device implantation enabled the extraction of blood and explantation of organs including liver, spleen, heart, kidney, brain and lung. Charles River Laboratory conducted complete blood count and blood chemistry tests on the blood samples collected in K-EDTA and gel tubes, respectively. Weighing, splitting the explanted organs in half and storing the halves in pre-weighed 15 ml conical metal-free tubes at −20 °C or in 10% buffered formalin in 50 ml conical tubes prepared tissue samples for biodistribution and histology studies, respectively. The concentrations of Si in the tissues at 1, 3 and 5 weeks post-implanation were determined by dissolving the tissues by adding 1.5 ml nitric acid and 0.35 ml hydrogen peroxide to each tube; the tubes were then kept in a 65 °C water bath for 5 h before diluting 1:20 in Milli-Q water (MilliporeSigma). Samples were analysed by inductively coupled plasma optical emission spectrometry to demonstrate the biodistribution and biodegradability of the dissolved silicon.

Evaluation in animal models. All of the procedures of the animal study followed the recommendations in the Guide for the Care and Use of Laboratory Animals of the National Institutes of Health[37]. The Institutional Animal Care and Use Committee (IACUC) of Washington University in St Louis approved the protocol (protocol no. 20170189). Male Lewis rats weighing 250–350 g (Charles River) received subcutaneous injections of buprenorphine hydrochloride (0.05 mg kg^{-1}; Reckitt Benckiser Healthcare) for pain management and of ampicillin (50 mg kg^{-1}; Sage Pharmaceuticals) to prevent infection at the implantation site before the surgical process. The surgical procedures involved anaesthetizing the rat with isoflurane gas, holding the head in a stereotaxic frame, opening a craniectomy and dura, implanting the bioresorbable sensor on the cortical surface and sealing the craniectomy with a PLGA sheet (~10 μm thick) and bioresorbable glue (TissueSeal). A clinical intracranial pressure monitor (Camino System, Model MPM-1; Integra LifeSciences) or a commercial thermistor (DigiKey) implanted in a nearby craniectomy enabled comparison testing to demonstrate the accuracy of the pressure and temperature measurements by the bioresorbable sensor, respectively. Bioresorbable glue sealed the opening for the commercial sensor after testing.

The set-up for wired data acquisition from bioresorbable sensor was as described above. Soldering the wires to plug connectors (DigiKey) and plugging formed an electrical connection between the bioresorbable sensor and a miniaturized wireless potentiostat (Supplementary Fig. 10b, right; Pinnacle Technology) to enable wireless data acquisition[8]. Pinnacle Acquisition Laboratory v.1.6.7 software was used for data collection. A plastic protector hat, secured to the rat's skull by transcranial screws (#0-80, 1/8" stainless steel screws; Component Supply) and dental cement (Fusio Liquid Dentin; Pentron), stored the device components for both wired and wireless modes throughout the monitoring period (Supplementary Figs. 10a–c).

Evaluation of the MRI compatibility. The experimental set-up in Fig. 5a consisted of a bioresorbable sensor and two fibre optic temperature probes (Luxtron 812 Fluoroptic Thermometer; LumaSense Technologies), one placed near the sensor and the other distant, sandwiched between two slabs of brain phantom (True Phantom Solutions). A 3 Tesla Siemens Magnetom Prisma MRI scanner performed a high specific absorption rate (or RF deposition) turbo spin echo scan (repetition time: 6,290.0 ms; echo time: 99 ms; 14 slices; thickness: 4 mm; flip angle: 180°; field

of view: 230 mm × 230 mm) continuously for 20 min. To assess the in vivo images for magnetic-susceptibility-related artefacts, a 4.7 Tesla Agilent Small-Animal MRI system captured gradient-echo images of a rat brain implanted with a bioresorbable sensor (with copper wire connections that terminate outside the sutures) in Fig. 5c (repetition time: 50 ms; echo time: 4.56 ms; five slices; thickness: 0.5 mm (no gap); flip angle: 20°, with 117 µm in-plane resolution (30 mm × 30 mm, 256 × 256 field of view); six signal averages and a total acquisition time of 1 min 17 s. Three independent experiments confirmed this trend.

Reporting Summary. Further information on research design is available in the Nature Research Reporting Summary linked to this article.

Data availability

The authors declare that all data supporting the findings of this study are available in the paper and its Supplementary Information.

Received: 16 April 2018; Accepted: 23 August 2018;
Published online: 1 October 2018

References

1. Jiang, G. Design challenges of implantable pressure monitoring system. *Front. Neurosci.* **4**, 29 (2010).
2. Yu, L., Kim, B. & Meng, E. Chronically implanted pressure sensors: challenges and state of the field. *Sensors* **14**, 20620–20644 (2014).
3. Sit, A. J. Continuous monitoring of intraocular pressure: rationale and progress toward a clinical device. *J. Glaucoma* **18**, 272–279 (2009).
4. Boutry, C. M. et al. Towards biodegradable wireless implants. *Phil. Trans. R. Soc. A* **370**, 2418–2432 (2012).
5. Chamis, A. L. et al. *Staphylococcus aureus* bacteremia in patients with permanent pacemakers or implantable cardioverter-defibrillators. *Circulation* **104**, 1029–1033 (2001).
6. Hall-Stoodley, L., Costerton, J. W. & Stoodley, P. Bacterial biofilms: from the natural environment to infectious diseases. *Nat. Rev. Microbiol.* **2**, 95–108 (2004).
7. Polikov, V. S., Tresco, P. A. & Reichert, W. M. Response of brain tissue to chronically implanted neural electrodes. *J. Neurosci. Methods* **148**, 1–18 (2005).
8. Kang, S.-K. et al. Bioresorbable silicon electronic sensors for the brain. *Nature* **530**, 71–76 (2016).
9. Luo, M., Martinez, A. W., Song, C., Herrault, F. & Allen, M. G. A microfabricated wireless RF pressure sensor made completely of biodegradable materials. *J. Microelectromech. Syst.* **23**, 4–13 (2014).
10. Hwang, S.-W. et al. Biodegradable elastomers and silicon nanomembranes/nanoribbons for stretchable, transient electronics, and biosensors. *Nano Lett.* **15**, 2801–2808 (2015).
11. Yu, K. J. et al. Bioresorbable silicon electronics for transient spatiotemporal mapping of electrical activity from the cerebral cortex. *Nat. Mater.* **15**, 782–791 (2016).
12. Lee, Y. K. et al. Dissolution of monocrystalline silicon nanomembranes and their use as encapsulation layers and electrical interfaces in water-soluble electronics. *ACS Nano* **11**, 12562–12572 (2017).
13. Lee, G. et al. Fully biodegradable microsupercapacitor for power storage in transient electronics. *Adv. Energy Mater.* **7**, 1700157 (2017).
14. Lee, C. H. et al. Wireless microfluidic systems for programmed, functional transformation of transient electronic devices. *Adv. Funct. Mater.* **25**, 5100–5106 (2015).
15. Tao, H. et al. Silk-based resorbable electronic devices for remotely controlled therapy and in vivo infection abatement. *Proc. Natl Acad. Sci. USA* **111**, 17385–17389 (2014).
16. Hwang, S.-W. et al. A physically transient form of silicon electronics. *Science* **337**, 1640–1644 (2012).
17. Hwang, S.-W. et al. High-performance biodegradable/transient electronics on biodegradable polymers. *Adv. Mater.* **26**, 3905–3911 (2014).
18. Kang, S.-K. et al. Dissolution behaviors and applications of silicon oxides and nitrides in transient electronics. *Adv. Funct. Mater.* **24**, 4427–4434 (2014).
19. Kang, S.-K. et al. Biodegradable thin metal foils and spin-on glass materials for transient electronics. *Adv. Funct. Mater.* **25**, 1789–1797 (2015).
20. Fang, H. et al. Ultrathin, transferred layers of thermally grown silicon dioxide as biofluid barriers for biointegrated flexible electronic systems. *Proc. Natl Acad. Sci. USA* **113**, 11682–11687 (2016).
21. Lee, Y. K. et al. Kinetics and chemistry of hydrolysis of ultrathin, thermally grown layers of silicon oxide as biofluid barriers in flexible electronic systems. *ACS Appl. Mater. Interfaces* **9**, 42633–42638 (2017).
22. Haddad, S. H. & Arabi, Y. M. Critical care management of severe traumatic brain injury in adults. *Scand. J. Trauma Resusc. Emerg. Med.* **20**, 12 (2012).
23. Wang, Q., Ding, J. & Wang, W. Fabrication and temperature coefficient compensation technology of low cost high temperature pressure sensor. *Sens. Actuat. A* **120**, 468–473 (2005).
24. Camino, G., Lomakin, S. M. & Lazzari, M. Polydimethylsiloxane thermal degradation Part 1. Kinetic aspects. *Polymer* **42**, 2395–2402 (2001).
25. Kanda, Y. A graphical representation of the piezoresistance coefficients in silicon. *IEEE Trans. Electron Devices* **29**, 64–70 (1982).
26. Lund, E. & Finstad, T. G. Temperature and doping dependency of piezoresistivity in p-type silicon. *MRS Proc.* **657**, EE5.13 (2000).
27. Norton, P. & Brandt, J. Temperature coefficient of resistance for p- and n-type silicon. *Solid-State Electron.* **21**, 969–974 (1978).
28. Bratton, S. L. Guidelines for the management of severe traumatic brain injury. VI. *Indications for intracranial pressure monitoring. J. Neurotrauma* **24**, S37–S44 (2007).
29. *Post Craniotomy Subdural Pressure Monitoring Kit. Model 110-4G* (Integra NeuroSciences, 2010).
30. Johanson, C. E. et al. Multiplicity of cerebrospinal fluid functions: new challenges in health and disease. *Cerebrospinal Fluid. Res.* **5**, 10 (2008).
31. Moghimi, S. M. & Patel, H. M. Serum-mediated recognition of liposomes by phagocytic cells of the reticuloendothelial system – the concept of tissue specificity. *Adv. Drug Deliv. Rev.* **32**, 45–60 (1998).
32. Gelabert-González, M. et al. The Camino® intracranial pressure device in clinical practice. Assessment in a 1000 cases. *Acta Neurochir.* **148**, 435–441 (2006).
33. Martínez-Mañas, R. M., Santamarta, D., de Campos, J. M. & Ferrer, E. Camino intracranial pressure monitor: prospective study of accuracy and complications. *J. Neurol. Neurosurg. Psychiat.* **69**, 82–86 (2000).
34. Zacchetti, L., Magnoni, S., Di Corte, F., Zanier, E. R. & Stocchetti, N. Accuracy of intracranial pressure monitoring: systematic review and meta-analysis. *Crit. Care* **19**, 420 (2015).
35. Dunn, J. F. et al. Functional mapping at 9.4T using a new MRI compatible electrode chronically implanted in rats. *Magn. Reson. Med.* **61**, 222–228 (2009).
36. Sawyer-Glover, A. M. & Shellock, F. G. Pre-MRI procedure screening: recommendations and safety considerations for biomedical implants and devices. *J. Magn. Reson. Imaging* **12**, 92–106 (2000).
37. National Research Council *Guide for the Care and Use of Laboratory Animals* 8th edn (The National Academies Press, 2011).

Acknowledgements

J.S. thanks G. Mensing and J. Maduzia at the Micro-Nano-Mechanical Systems Cleanroom (University of Illinois at Urbana–Champaign) for assistance with process development. J.S. acknowledges support from True Phantom Solutions Inc. with the preparation of brain phantoms for MRI compatibility tests. Y.X. acknowledges support from the Ryan Fellowship and the Northwestern University International Institute for Nanotechnology. L.T. acknowledges support from a Beckman Institute Postdoctoral Fellowship at UIUC. I.K. acknowledges support from Cancer Center Support grant no. P30 CA060553 (National Cancer Institute) awarded to the Robert H. Lurie Comprehensive Cancer Center. K.J.Y. acknowledges support from the National Research Foundation of Korea (grant nos. NRF-2017M1A2A2048880 and NRF-2018M3A7B4071109) and Yonsei University Future-leading Research Initiative of 2017 (grant no. RMS2 2018-22-0028). Y.H. acknowledges support from the NSF (grant nos. 1400169, 1534120 and 1635443).

Author contributions

J.S., W.B., Y.L., M.C., J.K., H.R., J.-K.C., S.-K.K., S.M.W., K.J.Y. and J.A.R. designed and fabricated the sensors. J.S., Y.L., M.C., H.R., J.Z. and Y.K.L. conceived and performed the dissolution studies. J.S., W.B., I.K. and M.P. performed the biodistribution, toxicity and histology studies. Y.Y., P.G., M.R.M. and W.Z.R. performed the in vivo ICP measurements and analysed data. Y.X. and Y.H. performed mechanical simulations. J.S., Y.Y., L.T., C.R.H., W.S. and S.-K.S. performed the CT and MRI studies. J.S., Y.Y., W.B., Y.X., W.Z.R. and J.A.R. wrote the manuscript.

Competing interests

The authors declare no competing interests.

Additional information

Supplementary information is available for this paper at https://doi.org/10.1038/s41551-018-0300-4.

Reprints and permissions information is available at www.nature.com/reprints.

Correspondence and requests for materials should be addressed to W.Z.R. or J.A.R.

Publisher's note: Springer Nature remains neutral with regard to jurisdictional claims in published maps and institutional affiliations.

nature research

Corresponding author(s): John A. Rogers and Wilson Z. Ray

Reporting Summary

Nature Research wishes to improve the reproducibility of the work that we publish. This form provides structure for consistency and transparency in reporting. For further information on Nature Research policies, see Authors & Referees and the Editorial Policy Checklist.

Statistical parameters

When statistical analyses are reported, confirm that the following items are present in the relevant location (e.g. figure legend, table legend, main text, or Methods section).

n/a	Confirmed	
☐	☒	The exact sample size (*n*) for each experimental group/condition, given as a discrete number and unit of measurement
☐	☒	An indication of whether measurements were taken from distinct samples or whether the same sample was measured repeatedly
☒	☐	The statistical test(s) used AND whether they are one- or two-sided *Only common tests should be described solely by name; describe more complex techniques in the Methods section.*
☐	☒	A description of all covariates tested
☒	☐	A description of any assumptions or corrections, such as tests of normality and adjustment for multiple comparisons
☐	☒	A full description of the statistics including central tendency (e.g. means) or other basic estimates (e.g. regression coefficient) AND variation (e.g. standard deviation) or associated estimates of uncertainty (e.g. confidence intervals)
☒	☐	For null hypothesis testing, the test statistic (e.g. *F*, *t*, *r*) with confidence intervals, effect sizes, degrees of freedom and *P* value noted *Give P values as exact values whenever suitable.*
☒	☐	For Bayesian analysis, information on the choice of priors and Markov chain Monte Carlo settings
☒	☐	For hierarchical and complex designs, identification of the appropriate level for tests and full reporting of outcomes
☒	☐	Estimates of effect sizes (e.g. Cohen's *d*, Pearson's *r*), indicating how they were calculated
☐	☒	Clearly defined error bars *State explicitly what error bars represent (e.g. SD, SE, CI)*

Our web collection on statistics for biologists may be useful.

Software and code

Policy information about availability of computer code

Data collection	Wired data acquisition (all data in main figures) — 'LabVIEW SignalExpress for DMM (2013)' software, available for download online, was used for collection of pressure and temperature data using digital multimeter (Model USB-4065) from National Instruments. Wireless data acquisition (Supplementary Fig. 10e, f) - Pinnacle Acquisition Laboratory v.1.6.7 (Pinnacle Technology, USA)
Data analysis	Microsoft Excel and OriginPro 9.1 were used for data analysis and plotting.

For manuscripts utilizing custom algorithms or software that are central to the research but not yet described in published literature, software must be made available to editors/reviewers upon request. We strongly encourage code deposition in a community repository (e.g. GitHub). See the Nature Research guidelines for submitting code & software for further information.

Data

Policy information about availability of data

All manuscripts must include a data availability statement. This statement should provide the following information, where applicable:

- Accession codes, unique identifiers, or web links for publicly available datasets
- A list of figures that have associated raw data
- A description of any restrictions on data availability

The authors declare that all data supporting the findings of this study are available within the paper and its Supplementary Information.

Field-specific reporting

Please select the best fit for your research. If you are not sure, read the appropriate sections before making your selection.

☒ Life sciences ☐ Behavioural & social sciences ☐ Ecological, evolutionary & environmental sciences

For a reference copy of the document with all sections, see nature.com/authors/policies/ReportingSummary-flat.pdf

Life sciences study design

All studies must disclose on these points even when the disclosure is negative.

Sample size	No sample size calculation was performed. A sample size of 10 provided sufficient information for tracking changes in the thicknesses of the oxide layers (Fig. 2a), as both thickness and rate of dissolution of oxide films are highly uniform. Sample size of 2 (mice) helped check the repeatability of biodistribution and blood-test data (Figs. 3a,c and d).
Data exclusions	No data were excluded.
Replication	Data on in vitro and in vivo pressure measurements and in vitro dissolution studies were tested >3 times to ensure replicability. The results were replicable.
Randomization	All devices and animals tested were selected randomly.
Blinding	No blinding was necessary as there were no variations in animal tested in Figs. 3–5 (all mice and rats were healthy).

Reporting for specific materials, systems and methods

Materials & experimental systems

n/a	Involved in the study
☒	☐ Unique biological materials
☒	☐ Antibodies
☒	☐ Eukaryotic cell lines
☒	☐ Palaeontology
☐	☒ Animals and other organisms
☒	☐ Human research participants

Methods

n/a	Involved in the study
☒	☐ ChIP-seq
☒	☐ Flow cytometry
☐	☒ MRI-based neuroimaging

Animals and other organisms

Policy information about studies involving animals; ARRIVE guidelines recommended for reporting animal research

Laboratory animals	Fig. 3 — female CD-1 mice from Charles River weighing 20–25 grams, 6–15 weeks old at the time of implant Fig. 4, 5c — male Lewis rats from Charles River weighing 250–350 grams, 10–12 weeks old at the time of implant
Wild animals	This study did not involve wild animals.
Field-collected samples	This study did not involve samples collected from the field.

Magnetic resonance imaging

Experimental design

Design type	N/A. Non-fMRI
Design specifications	N/A
Behavioral performance measures	N/A

Acquisition

Imaging type(s)	Structural, T2*-weighted
Field strength	4.7 Tesla
Sequence & imaging parameters	The data shown in Figure 5c are multi-slice gradient echo images: TR = 50 ms, TE = 4.56 ms, 5 slices, thickness = 0.5 mm (no gap), flip angle = 20 degrees, with 117 um in-plane resolution (30 x 30 mm^2, 256 x 256 field-of-view). Six signal-averages were acquired for a total acquisition time of 1 min, 17 seconds. [Subsequently (five days after the images shown in Fig 5c) imaging of this same animal was repeated with TR = 125 ms, 30 degree flip-angle, and a range of TE (5, 10, 15, 20 ms), 117 um in-plane resolution (30 x 30 mm^2, 256 x 256 field-of-view), 16 averages. The longer echo time would intensify any susceptibility-related image artifacts, but still no such artifacts were observable.
Area of acquisition	Scout images were acquired to locate the position of the sensor implant. On the basis of the scout images we planned a set of higher-resolution axial, coronal, and sagittal images of the brain to include the implanted sensor.

Diffusion MRI ☐ Used ☒ Not used

Preprocessing

Preprocessing software	N/A
Normalization	N/A
Normalization template	N/A
Noise and artifact removal	N/A. The images shown are simple 2D Fourier transforms of the acquired k-space data.
Volume censoring	N/A

Statistical modeling & inference

Model type and settings	N/A
Effect(s) tested	Simple visual inspection of the images were used to see if we could identify any regions consistent with magnetic-susceptibility artifacts (signal voids extending beyond the region of the sensor implant).

Specify type of analysis: ☒ Whole brain ☐ ROI-based ☐ Both

Statistic type for inference (See Eklund et al. 2016)	simple visual inspection
Correction	N/A

Models & analysis

n/a	Involved in the study
☒	☐ Functional and/or effective connectivity
☒	☐ Graph analysis
☒	☐ Multivariate modeling or predictive analysis